Draft version April 14, 2017
Preprint typeset using LaTeX style emulateapj v. 01/23/15

arXiv:1607.08247v2 [astro-ph.GA] 12 Apr 2017

ON THE DECREASING FRACTION OF STRONG LYα EMITTERS AROUND $z \sim$ 6-7

Raphael Sadoun[1], Zheng Zheng[1], and Jordi Miralda-Escudé[2,3]

Draft version April 14, 2017

ABSTRACT

The fraction of galaxies with strong Lyα emission has been observed to decrease rapidly with redshift at $z \gtrsim 6$, after a gradual increase at $z < 6$. This has been interpreted as a hint of the reionization of the intergalactic medium (IGM): the emitted Lyα photons would be scattered by an increasingly neutral IGM at $z > 6$. We study this effect by modeling the ionization and Lyα radiative transfer in the infall region and the IGM around a Lyα emitting galaxy (LAE), for a spherical halo model with the mean density and radial velocity profiles in the standard ΛCDM cosmological scenario. We find that the expected fast increase of the ionizing background intensity toward the end of the reionization epoch implies a rapid evolution of halo infall regions from being self-shielded against the external ionizing background to being mostly ionized. Whereas self-shielded infall regions can scatter the Lyα photons over a much larger area than the commonly used apertures for observing LAEs, the same infalling gas is no longer optically thick to the Lyα emission line after it is ionized by the external background, making the Lyα emission more compact and brighter within the observed apertures. Based on this simple model, we show that the observed drop in the abundance of LAEs at $z > 6$ does not imply a rapid increase with redshift of the fraction of the whole IGM volume that is atomic, but is accounted for by a rapid increase of the neutral fraction in the infall regions around galaxy host halos.

Subject headings: dark ages, reionization, first stars — galaxies: high-redshift — intergalactic medium — methods: analytical — radiative transfer

1. INTRODUCTION

Cosmic reionization corresponds to the last major phase transition of the universe during which the intergalactic medium (IGM) transitioned from a highly neutral to a highly ionized state. The detailed history of how reionization proceeded is still poorly constrained owing to the limited number of observational tools to probe neutral gas in the early universe (e.g., reviews by Miralda-Escudé 2003; Barkana & Loeb 2007; Ferrara & Pandolfi 2014). The Gunn-Peterson troughs (Gunn & Peterson 1965) observed blueward of the Lyα transition in the spectra of high-redshift quasars indicates that reionization was largely completed by $z \sim 6$ (e.g., Fan et al. 2002; White et al. 2003; Fan et al. 2006; Becker et al. 2007, 2015). Constraints on reionization at $z \gtrsim 6$ can be obtained from measurements of the Thomson scattering optical depth, $\tau_{\rm ts}$, using cosmic microwave background (CMB) data. As $\tau_{\rm ts}$ depends on the number density of free electrons integrated along the line-of-sight, it can be used to infer a characteristic reionization redshift $z_{\rm reion}$ but is insensitive to the precise reionization history. The latest results from the polarization data of the Planck satellite's Low Frequency Instrument and CMB lensing indicate a value $\tau_{\rm ts} = 0.066 \pm 0.013$ (Planck Collaboration et al. 2015), and those from the High Frequency Instrument give $\tau_{\rm ts} = 0.055 \pm 0.009$ (Planck Collaboration et al. 2016a), corresponding to a mean reionization redshift of $z_{\rm reion} \sim 7.8$–8.8 (Planck Collaboration et al. 2016b).

Lyα emitting galaxies, or Lyα emitters[4] (LAEs) constitute a promising alternative for studying neutral gas at early times and can provide important constraints on the late stages of reionization at $z \sim 6 - 7$ (see e.g., a recent review by Dijkstra 2014). LAEs are young star-forming galaxies in which most of the ionizing photons emitted from hot stars are converted to Lyα photons after recombinations in the interstellar medium (ISM), resulting in strong Lyα emission. As such, they have been predicted to be primary targets in the search for high-redshift galaxies (Partridge & Peebles 1967). After Lyα photons escape the interstellar medium around the young stars where they are produced, they experience resonant scattering by neutral hydrogen atoms in the surrounding IGM. The Lyα line emitted from these galaxies therefore contains information on the state of the neutral gas in their vicinity.

Before reionization was complete, an absorption imprint should be left on the Lyα emission line of LAEs because of the remaining atomic hydrogen in the IGM. The damped absorption wings of IGM regions with a high neutral fraction are expected to substantially suppress the Lyα emission lines of galaxies behind them (e.g., Miralda-Escudé & Rees 1998; Miralda-Escudé 1998). Recent observations of Lyα emitting galaxies at high redshift have indeed revealed a reduction in the visibility of LAEs between $z \sim 6$ and 7. Using ultra-deep narrow-band imaging with the Subaru telescope, Konno et al. (2014) found a rapid decline in the Lyα luminosity function (LF) of LAEs from $z = 6.6$ to 7.3. Combined with evidence for no evolution in the ultra-violet (UV) contin-

raphael.sadoun@utah.edu
[1] Department of Physics and Astronomy, University of Utah, 115 South 1400 East, Salt Lake City, UT 84112, USA
[2] Institució Catalana de Recerca i Estudis Avançats, Barcelona, Catalonia
[3] Institut de Ciències del Cosmos, Universitat de Barcelona (IEEC-UB), Barcelona, Catalonia

[4] Lyα emitters usually only refer to galaxies *selected* to have strong Lyα emission in narrow-band surveys. In this paper, we use the term Lyα emitters more generally for any galaxy with detectable Lyα emission

uum LF over the same redshift interval, they concluded that reionization is likely not complete at $z \sim 7$ and that this may explain the sudden decline of the Lyα LF of LAEs. The Lyα fraction $X_{\rm Ly\alpha}$, defined as the fraction of objects with strong Lyα emission among Lyman Break Galaxies (LBGs), is slowly rising from $z \sim 3$ to 6 (e.g., Stark et al. 2011), but then decreases suddenly between $z \sim 6$ and 7 (Fontana et al. 2010; Stark et al. 2010; Pentericci et al. 2011; Ono et al. 2012; Schenker et al. 2012; Caruana et al. 2014; Schmidt et al. 2016). Although one can imagine evolution models for intrinsic galaxy properties such as the escape fraction of ionizing photons or the dust content that might explain this drop in observed Lyα emission (e.g., Dayal & Ferrara 2012), the fraction $X_{\rm Ly\alpha}$ should not decline in a synchronized way for all galaxies in the Universe over a narrow time interval (note that $\Delta z = 1$ corresponds to less than ~ 200 Myr at $z \sim 6$, or $\sim 20\%$ of the age of the Universe at that epoch), so this decline has naturally been interpreted as a signature of the increase in the neutral gas fraction in the IGM towards high redshift.

The main difficulty with the simple scenario where a smooth IGM at the end of the reionization epoch is causing this drop of LAEs is that, adopting a simple attenuation model for the transmission of the Lyα line through the intervening IGM, the observed drop in $X_{\rm Ly\alpha}$ between $z = 6$ and $z = 7$ implies a rapid evolution in the volume-averaged neutral fraction $\langle x_{\rm HI} \rangle$ of several tens of percent (Pentericci et al. 2011; Dijkstra 2014). This would demand a late and very sudden reionization scenario, implying a surprisingly rapid rise in the emission rate of ionizing photons, and in tension with the Thomson scattering optical depth measurements by the *Wilkinson Microwave Anisotropy Probe* (WMAP; $z_{\rm reion} \sim 10.5$ derived in Hinshaw et al. 2013), although the latest results from Planck (Planck Collaboration et al. 2015, 2016a,b) have eased the tension with a late reionization.

For this reason, alternative scenarios have been proposed to explain the reduction in Lyα flux at $z \sim 6-7$ without requiring large variations in the neutral gas content of the IGM over this redshift interval.

Bolton & Haehnelt (2013) suggested that the transmission of the Lyα line might be significantly reduced due to the presence of relatively dense and neutral gas absorbers that are self-shielded against ionizing radiation. The size of these absorbers is reduced as the intensity of the ionizing UV radiation background rises. During the late stages of reionization, the mean free path of ionizing UV photons can increase rapidly as the self-shielded absorbers shrink, causing a rapid change in the ionizing background intensity (Miralda-Escudé et al. 2000; Giallongo et al. 2015; Madau & Haardt 2015; Mitra et al. 2016; Muñoz et al. 2016). As a consequence, the Lyα transmission through the intervening IGM might be reduced significantly without requiring a large change in $\langle x_{\rm HI} \rangle$ from $z = 6$ to $z = 7$. However, using results from reionization simulations, Mesinger et al. (2015) showed that these self-shielded absorbers cannot fully account for the total IGM opacity required to explain the observed drop in $X_{\rm Ly\alpha}$.

In general, the resonant nature of the Lyα line makes it difficult to infer the neutral state of the IGM surrounding LAEs directly from the evolution of $X_{\rm Ly\alpha}$, as radiative transfer effects can significantly alter the transmission of the line (e.g., Zheng et al. 2010). In this paper, we aim to further explore the impact of a rapidly evolving ionizing UV background intensity on the visibility of LAEs at $z \sim 6-7$, taking into account radiative transfer effects. Compared to the previous scenarios mentioned above, we focus our investigation on how the distribution of neutral gas surrounding the LAEs *themselves* is affected by the local UV background when taking into account self-shielding effects. Furthermore, we calculate the full radiative transfer of Lyα photons using a Monte-Carlo approach in order to accurately predict the Lyα properties resulting from the transmission through this gas. For this purpose, we use an analytical description to model the gas distribution and kinematics around LAEs at high-redshift. As the radiative transfer of the Lyα line can be significantly modified depending on the gas kinematics, we also explicitly consider inflow of gas onto the host LAE halo.

The paper is organized as follows. In Section 2, we describe our model for the gas distribution around high-z LAEs, and present the details of the self-shielding and Lyα radiative transfer calculations. The Lyα properties of our modeled LAEs as well as the main results on the evolution of the Lyα fraction are presented in Section 3. Finally, we discuss the implications of our results and conclude in Section 4.

2. LAE MODEL

In this section, we start by presenting the analytical model we use for the density and velocity of the gas surrounding LAEs. Then, we describe how the self-shielding effect is taken into account to calculate the corresponding neutral gas distribution in the presence of an external ionizing UV background. Finally, we present the radiative transfer calculations used to predict the Lyα properties from our model.

2.1. *Gas Density and Velocity*

Our model assumes that an LAE is in the center of a dark matter halo of virial mass M_h, with a gas distribution that is modeled in terms of the dark matter distribution. We assume a dark matter density profile within the virial radius of the halo, r_h, described by the Navarro-Frenk-White (NFW) profile (Navarro et al. 1997),

$$\rho_{\rm NFW}(r) = \frac{\delta_c \rho_{\rm crit}(z)}{r/r_s(1+r/r_s)^2}, \tag{1}$$

where δ_c is a characteristic overdensity, r_s is the scale radius of the halo, $\rho_{\rm crit}(z) = 3H(z)^2/8\pi G$ is the critical density of the universe at redshift z, and $H(z)$ is the Hubble constant at redshift z. Throughout this paper, we adopt the WMAP-9 cosmology (Hinshaw et al. 2013) with $\Omega_m = 0.28$, $\Omega_\Lambda = 0.72$, $\Omega_b = 0.046$ and $H_0 = 70\,{\rm km/s/Mpc}$.

Both parameters δ_c and r_s can be expressed in terms of the halo virial mass M_h and concentration parameter $c_{\rm NFW} \equiv r_h/r_s$, where r_h is the halo virial radius. In this paper, halos are defined as to have a mean density of $\Delta \times \rho_{\rm crit}(z)$ within the virial radius r_h, which gives

$$r_h = \left(\frac{3M_h}{4\pi\Delta\rho_{\rm crit}(z)} \right)^{1/3} \tag{2}$$

and

$$\delta_c = \frac{\Delta}{3} \frac{c_{\rm NFW}^3}{\ln(1+c_{\rm NFW}) - c_{\rm NFW}/(1+c_{\rm NFW})}. \quad (3)$$

We choose $\Delta = 18\pi^2$ for the density contrast as a good approximation to the value predicted by the spherical collapse model for a flat ΛCDM cosmology at $z \gtrsim 6$ (Bryan & Norman 1998). We fix $c_{\rm NFW} = 2$ (about that of a Milky-Way sized halo at $z \sim 6-7$) and neglect its weak dependence on halo mass.

The gas distribution inside the halo should differ from that of the dark matter for several reasons. First, for constant gas temperature, the gas pressure flattens the distribution near the center, compared to the diverging NFW profile. Second, the gas can cool, settle in a disk and form stars, which will affect the rest of the gas due to ionization and supernovae. Moreover, the neutral gas distribution, which is the one relevant for Lyα transfer, is different from the total gas one because of photoionization and density and temperature variations. These effects are highly complex but, as we shall see below, the Lyα properties of our model LAEs depend mostly on the gas distribution outside the halo virial radius. We therefore ignore these complications at small radius, and simply impose a constant density core of radius $r_{\rm core} = \alpha r_h$. Exterior to this core radius, we assume the gas follows the NFW profile with density $\rho_{\rm gas} = f_b \rho_{\rm NFW}(r)$, where $f_b = \Omega_b/\Omega_m$ is the global baryon fraction, and interior to the core radius we have $\rho_{\rm gas} = f_b \rho_{\rm NFW}(r_{\rm core})$. In our fiducial model, we use $\alpha = 0.25$ as a rough estimate for the scale at which the gas stops following the underlying dark matter distribution. We examined the effect of varying the value of α (Appendix A) and found that it has little impact on our results since, again, the Lyα properties are mainly affected by the gas distribution outside of the halo that suffers from the self-shielding correction.

The gas distribution outside the halo and in the IGM is assumed to trace that of the dark matter. To describe the dark matter distribution, we apply the infall model of Barkana (2004), which predicts the average density and velocity profile around virialized structures of mass M_h at a given redshift z in the presence of infalling matter. Briefly, the model calculates the initial density profile around overdense regions in the density field linearly extrapolated to the present day using the extended Press-Schechter formalism (Press & Schechter 1974; Bond et al. 1991). The relation to the density and velocity profiles around virialized halos at a given redshift z is then established based on the spherical collapse, taking into account the effect of matter infall onto the halo. The model also predicts the 1σ scatter around the average profiles expected in the matter distribution around halos, which allows us to quantify the variations in the Lyα properties caused by the distribution of gas environment in the IGM. Note that this model has also been used by Dijkstra et al. (2007) to model the IGM to study the Lyα transmission at $z \gtrsim 6$.

At a certain radius $r_{\rm eq}$, the matter density $\rho_{\rm infall}$ given by the infall model reaches that given by the NFW profile $\rho_{\rm NFW}$. We find that $r_{\rm eq} \sim 2r_h$ for halo masses in the range 10^{10}–$10^{12} M_\odot$ considered in this work. The gas density profile in our model is then set to be $\rho_{\rm gas} = f_b \rho_{\rm NFW}(r_{\rm core})$ for $r \le r_{\rm core}$, $f_b \rho_{\rm NFW}(r)$ for $r_{\rm core} < r \le r_{\rm eq}$, and $f_b \rho_{\rm infall}(r)$ for $r > r_{\rm eq}$. We also set the maximum radius of the gas halo to be $10r_h$, for the purpose of computing the emerging Lyα spectrum.

For the velocity distribution of gas, we assume that it follows that of the dark matter outside of the virial radius of the halo, which accounts for the gas infall. Inside the virial radius, we assume that the gas is supported by dispersion with no bulk motion. We impose a smooth transition between the dispersion-dominated region (inside the virial radius) and the infall region (the surrounding IGM) and express the peculiar velocity v_p of the gas as

$$v_p(x) = \frac{v_{\rm infall}(x)}{1 + e^{-w(x-x_0)}}, \quad (4)$$

where $x = r/r_h$. The parameters w and x_0 control respectively the width and location of the transition between the two regimes. In the present model, we use $w = 20$ and $x_0 = 1$, which produces a sharp transition at the virial radius. For the total velocity $v_{\rm tot}$ of the gas, the contribution from the Hubble flow $v_{\rm Hubble}$ is added, i.e., $v_{\rm tot} = v_p + v_{\rm Hubble}$.

The top and bottom panels of Figure 1 show the resulting density and velocity profiles for a $z = 7$ halo of mass $M_h = 10^{10.5} M_\odot$, the typical mass of LAE host halos at $z \gtrsim 6$ as inferred from clustering analysis (Ouchi et al. 2010; Sobacchi & Mesinger 2015). The virial radius of the halo at this redshift is $r_h \sim 13\,$kpc (physical). The vertical dotted and dashed lines represent respectively the core and virial radius of the halo. The shaded regions represent the scatter expected in the total gas density and velocity profiles as predicted by the infall model. The total mean gas density is plotted in the top panel as the solid black curve, while the horizontal dashed line marks the mean baryonic density of the Universe. Note that the density predicted by the infall model falls off asymptotically towards the mean value. The total IGM radial velocity is negative (indicating infall) below the turnaround radius, which occurs at $r \sim 6r_h$ (indicated by the vertical dot-dashed line in the bottom panel; this agrees with results of numerical simulations, e.g., in Meiksin et al. 2014), and asymptotically approaches the Hubble flow at larger radius.

To summarize, at a given redshift z, our model describing the gas density and velocity distribution in the halo and the IGM depends only on a single parameter, the halo virial mass M_h. Throughout the paper, we assume a fixed value of $z = 7$ for all the calculations. The main reason for this choice is to isolate the effects of varying the intensity of the ionizing background while keeping the other parameters fixed. In practice, through tests we have verified that including the redshift dependence in our model does not affect our main conclusions on the evolution of the fraction of strong LAEs. We convert the gas density to hydrogen number density by $n_{\rm H} = X_{\rm H} \rho_{\rm gas}/m_{\rm H}$, where $X_{\rm H} = 0.76$ is the hydrogen mass fraction and $m_{\rm H}$ is the mass of the hydrogen atom.

2.2. *Self-Shielding Calculation*

For the Lyα radiative transfer, we need to know the neutral hydrogen distribution. With the gas distribution in Section 2.1, we solve the neutral hydrogen distribution by accounting for the self-shielding effects in the presence of a uniform external ionizing background as well as the

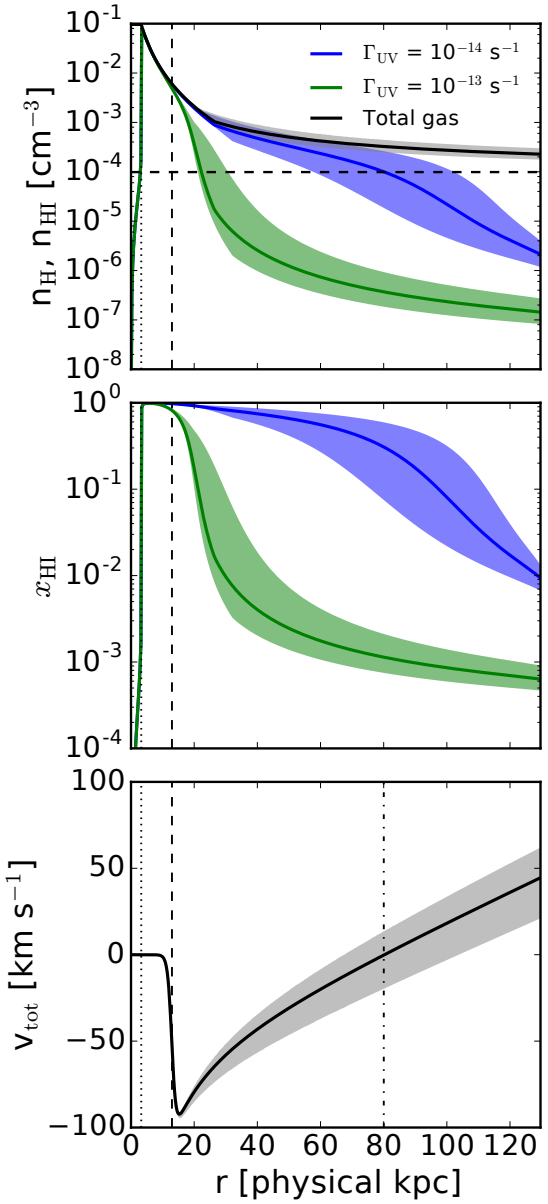

FIG. 1.— Gas density and velocity profiles of our fiducial LAE model for a halo of mass $M_h = 10^{10.5}\,\mathrm{M}_\odot$ and virial radius $r_h \sim 13\,\mathrm{kpc}$ at $z = 7$. Top panel shows the density profile of the total (black line) and neutral (blue and green lines) hydrogen gas. The neutral gas profiles are obtained by calculating the self-shielding effects in the presence of a uniform external ionizing background, with corresponding photoionization rates $\Gamma_{UV} = 10^{-13}\,\mathrm{s}^{-1}$ (green) and $\Gamma_{UV} = 10^{-14}\,\mathrm{s}^{-1}$ (blue), respectively. The horizontal dashed line represents the mean baryonic density of the universe. The middle panel shows the corresponding neutral hydrogen fractions $x_{HI} \equiv n_{HI}/n_H$. The bottom panel shows the total bulk velocity of the gas, where the vertical dot-dashed line marks the turnaround radius (see text). In all panels, the shaded region around each average profile shows the scatter resulting from the distribution of the IGM environment predicted by the infall model. The vertical dotted and dashed lines represent respectively the core radius of the gas distribution and the virial radius of the halo.

ionizing flux from the LAE at the center, following the approach in Zheng & Miralda-Escudé (2002) with an iterative procedure (Tajiri & Umemura 1998). The neutral fraction $x_{HI}(r) \equiv n_{HI}(r)/n_H(r)$ at a given distance r from the center of the cloud is found by solving the photonionization equilibrium equation,

$$x_{HI}(r)\Gamma_{tot,ss}(r) = \alpha_B(T)\,[1 - x_{HI}(r)]\,n_e, \qquad (5)$$

where $\Gamma_{tot,ss}$ is the *total* attenuated photoionization rate, α_B is the case-B recombination coefficient at temperature T, and n_e is the electron number density. We assume a temperature of $T = 10^4\,\mathrm{K}$ ($\alpha_B = 2.35 \times 10^{-13}\,\mathrm{cm}^3\,\mathrm{s}^{-1}$). For the electron density, we account for the contribution from singly ionized helium with the same neutral fraction as hydrogen. With a helium mass fraction of $Y_{He} = 0.24$, we have $n_e = (1 - x_{HI})\,0.82\rho_{gas}/m_H$.

The total photoionization rate is the sum of the contributions from the central LAE source and the external UV background, $\Gamma_{tot,ss} = \Gamma_{LAE,ss} + \Gamma_{UV,ss}$. Assuming that ionizing photons are escaping isotropically from the LAE, the photoionization rate $\Gamma_{LAE,ss}$ at a distance r can be expressed as

$$\Gamma_{LAE,ss}(r) = \int_{\nu_L}^{\infty} \frac{f_{esc} L_\nu e^{-\tau_{\nu,cen}}}{4\pi r^2 h\nu} a_\nu d\nu, \qquad (6)$$

where ν_L is the H I Lyman limit frequency, $\tau_{\nu,cen}$ is the photoionization optical depth from the *center of the gas cloud* to r, a_ν is the photoionization cross-section of hydrogen at frequency ν, L_ν is the specific (ionizing) luminosity of the LAE and f_{esc} is the escape fraction of ionizing photons. We assume that the galaxy spectrum is of the form $L_\nu \propto \nu^{-\beta}$ for $\nu > \nu_L$ and that the total emission rate of ionizing photons Q is related to the instantaneous star formation rate (SFR) and the metallicity Z (in solar units) by

$$\log_{10} Q = 53.8 + \log_{10}(\mathrm{SFR}/M_\odot\,\mathrm{yr}^{-1}) - 0.0029(9 + \log_{10} Z)^{2.5}, \qquad (7)$$

which assumes constant SFR and a Salpeter IMF (Schaerer 2003; Dijkstra et al. 2007). We relate SFR to halo mass using the relation (Zheng et al. 2010)

$$\mathrm{SFR} = 0.68[M_h/(10^{10}h^{-1}\mathrm{M}_\odot)]\,\mathrm{M}_\odot\,\mathrm{yr}^{-1}. \qquad (8)$$

For our fiducial model, we assume solar metallicity ($Z = 1$), an escape fraction of ionizing photons from the central star-forming region of $f_{esc} = 0.1$, and $\beta = 3$, which results in a total emission rate of $Qf_{esc} \simeq 2 \times 10^{52}$ photons/s for a halo of mass $M_h = 10^{10.5}\,M_\odot$, using equations 7 and 8.

Given the intensity I_ν of the external ionizing background, the photoionization rate $\Gamma_{UV,ss}$ is computed as

$$\Gamma_{UV,ss} = \int_{4\pi} d\Omega \int_{\nu_L}^{\infty} \frac{I_\nu e^{-\tau_{\nu,out}}}{h\nu} a_\nu d\nu, \qquad (9)$$

where $\tau_{\nu,out}$ is the photoionization optical depth from *outside the cloud* to r along a given direction. The integration over the solid angle accounts for ionizing photons coming from all directions to the position at r. We assume that the ionizing background intensity I_ν is a constant, denoted as $I_{\nu,0}$, between ν_L and $4\nu_L$, and zero above $4\nu_L$ (the He II Lyman limit). The constant $I_{\nu,0}$ is a parameter of our model and is chosen such that it gives the desired value of the photoionization rate Γ_{UV} of the ionizing background when computed in the optically thin regime ($\tau_\nu << 1$). Since the redshift evolution of Γ_{UV} is still poorly constrained at $z \geq 6$, we consider two typical

cases in our fiducial model with $\Gamma_{\rm UV} = 10^{-13}\,{\rm s}^{-1}$ and $10^{-14}\,{\rm s}^{-1}$, corresponding approximately to the expected evolution between $z = 6$ and $z = 7$ (Fan et al. 2006; Becker & Bolton 2013; Giallongo et al. 2015; Madau & Haardt 2015; Mitra et al. 2016; Muñoz et al. 2016).

The photoionization equilibrium equation is solved using an iterative method. First, the neutral fraction profile is initialized assuming the system to be optically thin to ionizing photons [$\tau_\nu << 1$ in equation (9)]. Then, at each consecutive iteration, the value of the optical depth τ_ν is recalculated in all directions according to the updated neutral gas distribution and the neutral fraction is solved using equation (5). The process is repeated until the neutral fraction has converged within a fractional error of less than 10^{-5}.

The top and middle panels of Figure 1 show respectively the neutral gas density and the corresponding neutral fraction profiles obtained for the $10^{10.5}\,M_\odot$ halo. The green and blue curves are for $\Gamma_{\rm UV} = 10^{-13}\,{\rm s}^{-1}$ and $\Gamma_{\rm UV} = 10^{-14}\,{\rm s}^{-1}$, respectively. The shaded regions show the expected scatter around the average, coming directly from the variation in the IGM environment predicted by the infall model. Note that we do not consider variations in the gas distribution inside the halo since, as mentioned previously, these have little effect on the resulting Lyα properties.

As expected, varying the ionizing background by one order of magnitude has a significant impact on the neutral gas distribution owing to the self-shielding effects. The main difference is seen in the ionization state of the infall region surrounding the halo for $r_h \lesssim r \lesssim 6r_h$. For $\Gamma_{\rm UV} = 10^{-14}\,{\rm s}^{-1}$, the gas in this region remains highly neutral, while it is highly ionized ($x_{\rm HI} \sim 10^{-3} - 10^{-2}$ at $r > 2r_h$) for $\Gamma_{\rm UV} = 10^{-13}\,{\rm s}^{-1}$. This can also be quantified in terms of the transition radius where $x_{\rm HI} = 0.5$. With the low UV background, this transition happens close to the turnaround radius, at $r \sim 5r_h$, while with the high UV background, the transition occurs in the vicinity of the halo virial radius, at $r \sim 1.3r_h$.

In both cases, the transition radius is larger than the virial radius of the halo, so the gas inside the virial radius is self-shielded against the external ionizing backgroung. Therefore, the gas in the infall region is the one that responds to a change in the external ionizing intensity for this range of Γ_{UV}, and determines the transfer of the emerging Lyα radiation and the visibility of LAEs.

The presence of the central source of ionizing photons does not substantially modify the neutral gas distribution of this infall region, for the ionizing central luminosity we have assumed. The reason is that the total recombination rate in the core region within $r_{\rm core} = 0.25r_h$ is $(4\pi/3)\,r_{\rm core}^3\alpha_B\,0.82n_H \simeq 2\times10^{52}$ photons/s, comparable to the total emission $Qf_{\rm esc}$. Therefore, the central source simply creates a central HII region that barely suffices to ionize the core, and does not affect the ionization structure of the outer regions, as seen in Figure 1. Had we assumed a larger central ionizing luminosity, the central source would of course have ionized completely the surrounding gas and the Lyα photons would then emerge with little scattering, drastically changing our predictions. Our model is therefore valid for halos in which the central source is not very luminous. In practice, we expect that there is a minority of halos in which a highly luminous source (either a quasar or a galaxy with an extremely high star-formation rate) completely ionizes the gas surrounding the halo (and then contributes to the reionization of the intergalactic medium), while in the majority of halos the internal sources are not capable of ionizing all the halo gas and the infall region needs to be ionized by the external ionizing background. As long as the full ionization of the gas inside the virial radius does not occur, the details of the gas distribution assumed within r_h should not impact our results on the transmission of the Lyα emission line (see Appendix A).

2.3. *Lyα Radiative Transfer*

With the density and velocity distribution of the neutral hydrogen gas in the model, we perform a Lyα radiative transfer calculation using a modified parallel version of the Monte-Carlo code from Zheng & Miralda-Escudé (2002a). The code numerically follows the trajectories of Lyα photons, which diffuse spatially and in frequency as they scatter in the model cloud. Lyα photons are launched at line center from the center of the gas halo and travel along a random direction until they are scattered. The location of the scattering event is obtained by drawing a random optical depth τ (following an exponential distribution) and computing the corresponding distance in the chosen direction. After each scattering, a new frequency and propagation direction of the photon are computed based on the velocity of the atom that scatters the photon. This scattering process is repeated until the photon escapes the gas cloud, at which point we record its frequency, its direction of propagation, and the location of the last scattering. We refer the reader to Zheng & Miralda-Escudé (2002a) for more details.

Following Zheng et al. (2010), we relate the Lyα luminosity of our model LAEs to their SFR,

$$L_{{\rm Ly}\alpha} = 10^{42}[{\rm SFR}/({\rm M}_\odot{\rm yr}^{-1})]\,{\rm erg\,s}^{-1}, \qquad (10)$$

where the SFR is related to halo mass using Equation 8. Our results on the influence of varying the ionizing background on the LAE fraction are not sensitive to the particular $L_{{\rm Ly}\alpha} - M_h$ relation, as shown later. The effective temperature for gas inside halos for the purpose of computing the Lyα radiative transfer is set to be $10^6\,{\rm K}$. This is different from the gas temperature $T = 10^4\,{\rm K}$ assumed for the self-shielding calculation, and is introduced to account for a realistic level of turbulent fluid motions in the infall region. One might expect variations in the predicted Lyα properties as we change the gas temperature for the radiative transfer calculations, given the impact of Doppler broadening on Lyα radiative transfer. By performing tests with the temperature set to $T = 10^4\,{\rm K}$, we found that the decrease in Lyα flux caused by the change in the UV background remains essentially the same as in our fiducial model and thus our final conclusion is not substantially affected.

We model LAEs in halos of $\log(M_h/M_\odot) = 10.0$ to $\log(M_h/M_\odot) = 12.0$ with a step size of 0.5 dex. For each halo mass, we consider 3 different IGM environments corresponding respectively to the average and $\pm1\sigma$ scatter in the gas density and velocity profiles predicted from the infall model in order to compute the scatter in the results. The number of photons we have numerically followed for each case is $N = 10^5$. We present the results from the radiative transfer calculation in the next section.

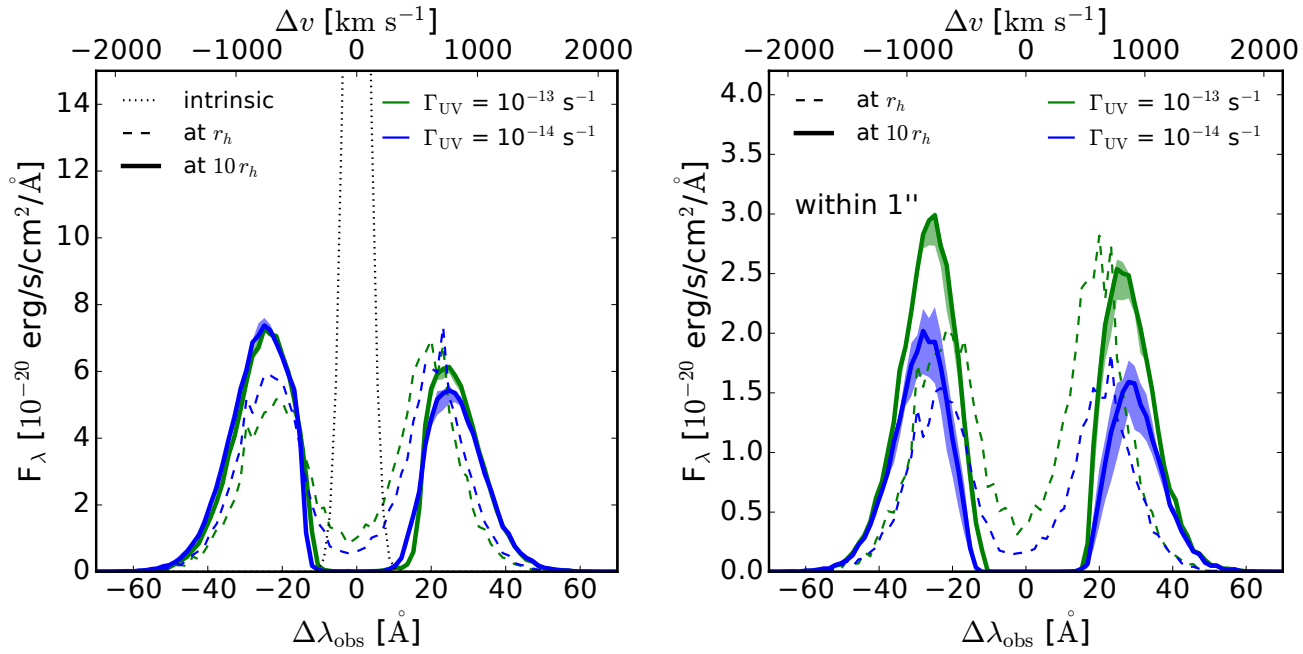

FIG. 2.— Flux per unit wavelength of the Lyα emission of a model LAE in halos of $M_h = 10^{10.5} M_\odot$, at $z = 7$. The spectra are obtained either for all photons (*left*) or only for photons escaping within projected radius of $1''$ from the central source (*right*). The bottom x-axis shows the offset with respect to the line center, expressed in the observer frame in wavelength units $\Delta\lambda_{\rm obs} = (1+z)\Delta\lambda$, while the top axis shows the offset in velocity units $\Delta v = c\,\Delta\lambda/1215.67\mathring{A}$. The solid lines are the predicted spectra when photons reach the outer radius of our radiative transfer calculation at $10r_h$, while the dashed lines are the spectra of photons reaching the virial radius of the halo r_h. The dotted black line is the intrinsic spectrum that would be observed if no radiative transfer effects were taken into account. The blue side of the spectra will be highly supressed through attenuation by the IGM far away from the source, and only the red side of the spectra is left to be observed (see text).

3. RESULTS

We now study the Lyα spectra and surface brightness profiles of our model LAEs, based on our radiative transfer calculations. Then, we present the main result of this paper on the evolution of the Lyα fraction at $z \gtrsim 6$.

3.1. *Lyα Spectra*

We record the location of last scattering as well as the frequency and direction of all Lyα photons when they escape the gas cloud at the outer radius of our radiative transfer calculation, which we have set at $10r_h$. This information enables us to compute the Lyα spectrum of an LAE at any projected radius. The left panel of Figure 2 shows the flux per unit wavelength of the photons as they come out of the cloud at $10r_h$, as the thick solid lines. The results are shown for a halo of mass $M_h = 10^{10.5} M_\odot$ at $z = 7$, and for the neutral gas distribution of the two ionizing background intensities that were used in Figure 1: $\Gamma_{\rm UV} = 10^{-13}\,{\rm s}^{-1}$ (green lines) and $\Gamma_{\rm UV} = 10^{-14}\,{\rm s}^{-1}$ (blue lines).

To gain physical insight into the effects of scattering by the hydrogen in the infall region on the emission line shape, we also record the frequency of photons as they first move out of the virial radius of the halo, r_h. These spectra are shown in the left panel of Figure 2 as the dashed lines, for the same two cases as the solid lines. The black, dotted line is the intrinsic emission profile of the central source assumed in our model. Note that the photon luminosity of the central source is the same in all cases, and all the emitted photons eventually escape after multiple scatterings, so the area under all five curves in the left panel is the same.

The resulting scattered spectra have the characteristic double-peak profile expected from a central point source within a static gas distribution (Neufeld 1990; Zheng & Miralda-Escudé 2002a; Dijkstra et al. 2006). When photons are scattered in a region with a negative radial velocity gradient (in our case, a narrow range around r_h; see bottom panel of Fig. 1), the red peak ($\Delta\lambda > 0$) acquires a greater intensity; this is seen clearly in the model of $\Gamma_{\rm UV} = 10^{-13}\,{\rm s}^{-1}$ in the left panel of Figure 2 (dashed green line), where the faster reduction of the neutral density with radius compared to the $\Gamma_{\rm UV} = 10^{-14}\,{\rm s}^{-1}$ case enhances the peak asymmetry that is produced. At radius r_h, an important fraction of the photons are still left between the two peaks. As photons diffuse further out into the region of positive radial velocity gradient, the effect is reversed and photons that are scattering between the two peaks are then more likely to end up in the blue peak ($\Delta\lambda < 0$). Overall, the radiative transfer through the infall region of the halo shifts most of the photons remaining near the central region of the line to the blue peak, and pushes the red peak further to the red, suppressing its intensity with respect to the blue one.

The spectra shown in this left panel of Figure 2 are not what is directly observed. Two effects need to be taken into account that further modify the spectrum. First, the apertures that are most often used to measure the spectrum are much smaller than the angular size of the outer radius of $10r_h$ at which we compute the emerging spectrum, which is $\sim 24''$ at $z = 7$. Second, these emerging photons will still undergo further scattering beyond the limiting radius $10r_h$ used in our calculation. In reality, photons in the blue peak should not be observed because,

as they travel to the observer, they will shift to the Lyα line center at a radius much larger than $10r_h$, and they will be scattered again and reemitted from a region of much larger angular size, and therefore with a very low surface brightness. On the other hand, photons in the red peak should not be further scattered after they have moved beyond $10r_h$. We have performed tests by extending the size of the cloud of gas to $30r_h$, which show that the blue component becomes highly suppressed, while the red component remains unchanged. Therefore we can include this second effect by simply assuming that only the red peak is observed, and the blue peak is completely suppressed by scattering in the IGM that is in Hubble expansion around the halo at $r > 10r_h$. Note that this simple treatment implicitly assumes that photons propagate in a smooth IGM after they reach the limit of the gas cloud in our model and does not take into account additional absorption from self-shielded (Lyman-limit) systems in a clumpy IGM at $r > 10r_h$. For this reason, the apparent drop in Lyα flux that we predict in our model (Section 3.2) should be considered as a lower limit to the total Lyα flux decrement produced by self-shielding effects.

To include the first effect, we now assume that the Lyα emission is observed with a circular aperture of radius $1''$, a typical aperture used for source extraction in narrow-band high-z LAE surveys. For each photon that reaches the outer radius $10r_h$, we compute the projected radius after its last scattering, $R = \sqrt{r_{\rm ls}^2 - (\boldsymbol{k} \cdot \boldsymbol{r}_{\rm ls})^2}$, where $\boldsymbol{r}_{\rm ls}$ is the vector position (with respect to the halo center) of the last scattering, and $\boldsymbol{k}$ is the unit vector along the photon escaping direction. The spectra of photons with R within the $1''$ aperture are shown in the right panel of Figure 2, for the two cases of $\Gamma_{\rm UV}$. Solid lines are the spectra of these photons as they exit the outer radius $10r_h$, and dashed lines show the spectrum these photons had when first moving out of r_h. Note that for this latter case, the projected radius is still computed after the escape from $10r_h$, and only the frequency is recorded at r_h, simply to show how the frequency of these photons has changed as a result of the radiative transfer through the infall region. The area under the two green curves is therefore the same, and so is the area under the two blue curves, but these areas are lower than in the left panels by a factor equal to the fraction of photons that are eventually emitted within the aperture of radius $1''$.

We can now clearly see the effect of having a self-shielded infall region around the halo of a LAE. For the more intense ionizing background (green lines), when self-shielding starts only near the virial radius r_h, the photons that escape in the red peak are unlikely to be scattered at a radius substantially larger than r_h and as a result the flux within the $1''$ aperture is suppressed by only a factor ~ 2.5 relative to the total flux in the red peak. However, when the ionizing background is weaker and the entire infall region is self-shielded (blue lines), most photons are scattered at a larger projected radius and the red peak is suppressed by a factor ~ 4. We note that, in both cases, more than half of the photons are scattered into the blue peak, similarly to the effect seen for all the photons in the left panel, but the variation in this blue peak fraction is small and is not related to the change in the Lyα visibility. The reason for the greater reduction of the observed Lyα line (i.e., the red peak) for the $\Gamma_{\rm UV} = 10^{-14}\,{\rm s}^{-1}$ case is the much more extended neutral hydrogen profile caused by self-shielding, which spreads the Lyα photons over a much larger area, therefore reducing the surface brightness and the detected flux within the small apertures used for observing the spectra.

Our model predicts an apparent Lyα line profile (the red peak of the spectra) with a velocity offset of $\sim 800 - 900\,{\rm km\,s}^{-1}$ with respect to the systemic redshift of the LAE. This is larger than the observed Lyα line profiles for which the offset is typically $\sim 100 - 450\,{\rm km\,s}^{-1}$ at $z \sim 2$ (Shibuya et al. 2014; Stark et al. 2014) and $\sim 200 - 500\,{\rm km\,s}^{-1}$ at $z \gtrsim 6$ (Willott et al. 2015). Even the velocity offsets in the predicted spectra emerging at r_h are already larger compared to the observed values which indicates that the neutral gas density inside the halo is probably overestimated in our model. This could be due to the relatively low escape fraction of ionizing photons that we assume in our fiducial model ($f_{\rm esc} = 0.1$). We have examined the effect of increasing the escape fraction by a factor of two in our model (see Appendix A) and found that it reduces the velocity offset to $\sim 550\,{\rm km\,s}^{-1}$, bringing it much closer to the observed value but without affecting the apparent flux reduction in the red peak when varying $\Gamma_{\rm UV}$.

3.2. *Lyα Surface Brigthness Profiles*

We now examine in more detail the variation in the Lyα surface brightness profile as the ionizing background decreases, producing a self-shielded infall region.

Figure 3 plots the Lyα surface brightness profiles for different halo masses spanning the range $10^{10} - 10^{12} M_\odot$. The cases for $\Gamma_{\rm UV} = 10^{-13}\,{\rm s}^{-1}$ and $\Gamma_{\rm UV} = 10^{-14}\,{\rm s}^{-1}$ are represented as solid and dashed lines, respectively. The curves show the average profiles, and the expected scatter around them caused by variations of the IGM gas distribution is shown only for the lowest and highest halo mass to avoid excessive cluttering.

As the ionizing background increases from $\Gamma_{\rm UV} = 10^{-14}\,{\rm s}^{-1}$ to $10^{-13}\,{\rm s}^{-1}$, the gas is ionized at smaller radius (see Figure 1) and Lyα photons suffer less spatial diffusion before escaping the cloud. This causes a steeper surface brightness profile, and a higher observed flux within a small aperture near the center.

The surface brightness profile shows a clear dependence on halo mass. As halo mass increases, the self-shielding radius shifts toward large radius and the neutral hydrogen column density within the self-shielded region increases. As a consequence, Lyα photons experience more scatterings and diffuse more spatially before entering the highly ionized, low density region. For $M_h = 10^{12} M_\odot$, the surface brightness profile becomes very flat out to more than 5 arcseconds, which is not consistent with observed LAEs. However, most LAEs at $z > 6$ are probably not hosted in these extremely massive halos. Our model is also unrealistic for the region inside the virial radius, where turbulent motions and gas clumpiness are likely to be present which would affect radiative transfer and the surface brightness profile. Nevertheless, the surface brightness profiles for the two cases of $\Gamma_{\rm UV}$ values in Figure 3 provides a reasonable indication for the ratio of Lyα emission intensities to be expected in the two models.

The dependence of the ratio of Lyα fluxes for the two

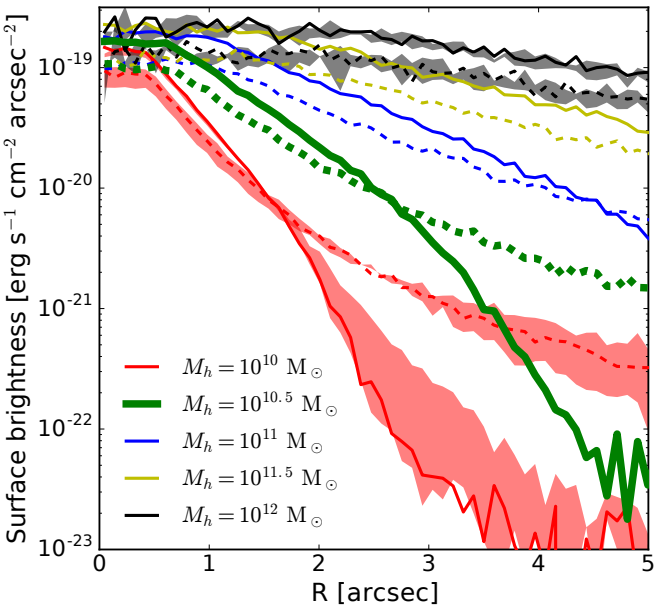

FIG. 3.— Lyα surface brightness profiles for model LAEs residing in halos of various masses. Solid lines and dashed lines are the profiles obtained for $\Gamma_{\rm UV} = 10^{-13}\,{\rm s}^{-1}$ and $\Gamma_{\rm UV} = 10^{-14}\,{\rm s}^{-1}$, respectively. For clarity, the scatter (shaded regions) resulting from variable IGM environments (see Fig. 1) is shown only for the lowest and highest halo mass.

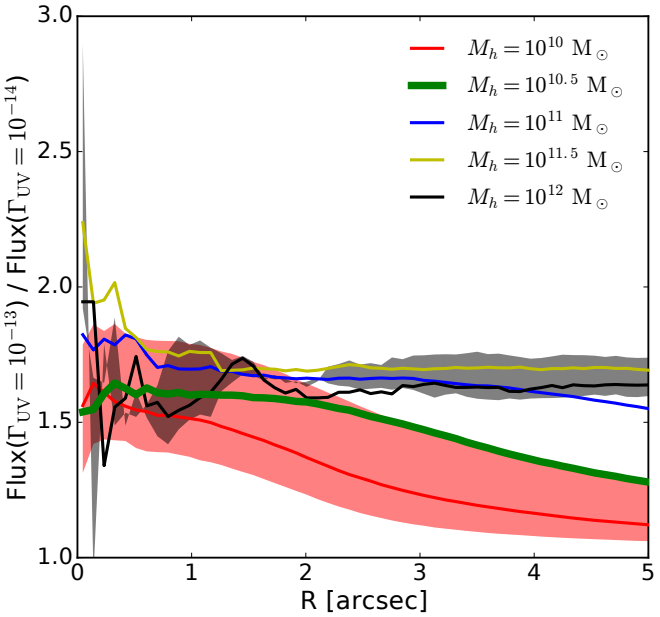

FIG. 4.— Lyα flux ratio as a function of aperture radius. The fluxes are computed by integrating the surface brightness profiles in Figure 3 out to R. For clarity, the scatter (shaded regions) caused by variations of IGM environments are only shown for the lowest and highest halo mass. At a fixed projected radius, there is a clear dependence of this ratio on the host halo mass, which translates into a luminosity-dependent effect on the observability of high-z LAEs.

cases ($\Gamma_{\rm UV} = 10^{-13}\,{\rm s}^{-1}$ and $10^{-14}\,{\rm s}^{-1}$) on the aperture radius R is shown in Figure 4. The total flux is computed by integrating the surface brightness profile out to R. For all halo masses, we find higher flux ratios at smaller aperture radii. With an aperture of $1''$ radius, the flux ratios are in the range $\sim 1.5 - 1.8$ and show a dependence on halo mass. The dependence of the flux ratio on halo mass shows a weak but interesting trend: for $M_h \lesssim 10^{11}\,{\rm M}_\odot$, the flux ratio increases with halo mass, but this trend is reversed at higher masses. This trend may help explain the observed evolution of the Lyα fraction at different galaxy luminosities, which we discuss next.

3.3. *Lyα Fraction Evolution*

Our model predicts an apparent Lyα flux decrease of LAEs in a small redshift interval caused by a fast change of the ionizing background intensity, which results in a rapid shrinkage of self-shielded regions in the infall zones around the host halos of LAEs. We now study how this affects the evolution of the Lyα fraction, $X_{\rm Ly\alpha}$, defined as the fraction of star-forming galaxies with a Lyα equivalent width above a certain threshold. As mentioned in the introduction, this fraction has been found to gradually increase up to $z = 6$, and then decline suddenly from $z = 6$ to 7 (see the compilation of data points in Figure 5). The Lyα fraction is expressed in terms of the equivalent width probability distribution $p(W)$ and the threshold W_t, as

$$X_{\rm Ly\alpha} = \int_{W_t}^{+\infty} p(W)\,{\rm d}W\ . \qquad (11)$$

For a direct comparison with observations, we consider two threshold values that have commonly been used, $W_t = 25$ Å and $W_t = 55$ Å. We also adopt the following parametrization for $p(W)$, motivated by the observed distribution at low redshifts (e.g., from $z \sim 3$ LBGs; Shapley et al. 2003):

$$p(W) = \begin{cases} 0 & \text{if } W \le -W_1, \\ 1/(W_0 + W_1) & \text{if } -W_1 < W \le 0, \\ \exp(-W/W_0)/(W_0 + W_1) & \text{if } W > 0\ , \end{cases} \qquad (12)$$

where W_0 and W_1 are two free parameters (note that W_1 is usually positive since a fraction of the galaxies have negative equivalent widths).

We now assume that $\Gamma_{\rm UV}$ drops from the high value of $10^{-13}\,{\rm s}^{-1}$ at $z = 6$, to the low value $10^{-14}\,{\rm s}^{-1}$ at $z = 7$, as an explanation of the fast drop in $X_{\rm Ly\alpha}$ between these two redshifts. We determine the values of W_0 and W_1 at $z = 6$ from the measured values of $X_{\rm Ly\alpha}$ at this redshift, using the two thresholds $W_t = 25$ Å and $W_t = 55$ Å. Hence, our model matches the data exactly at $z = 6$ by construction, and then predicts the drop at $z = 7$ as a function of the value of $\Gamma_{\rm UV}$.

Figure 5 shows the change of $X_{\rm Ly\alpha}$ from $z = 6$ to $z = 7$ in this model, compared to the observations, for the two equivalent width thresholds. Observational data points are taken from Stark et al. (2011), Curtis-Lake et al. (2012), Ono et al. (2012), Mallery et al. (2012), Schenker et al. (2012), Treu et al. (2013), Schenker et al. (2014), and Cassata et al. (2015), which provide constraints on $X_{\rm Ly\alpha}$ for both UV-faint ($M_{\rm UV} > -20.25$) and UV-bright ($M_{\rm UV} < -20.25$) galaxy samples. To compare the Lyα fraction evolution predicted by our model for these two samples, we therefore need to estimate the UV luminosity $L_{\rm UV}$ at a given halo mass. For this purpose, we adopt the $L_{\rm UV}$-SFR relation in Zheng et al. (2010) [their equation (5)]

$$L_{\rm UV} = 8 \times 10^{27}\,[{\rm SFR}/({\rm M}_\odot {\rm yr}^{-1})]\,{\rm erg\,s^{-1}\,Hz^{-1}}, \qquad (13)$$

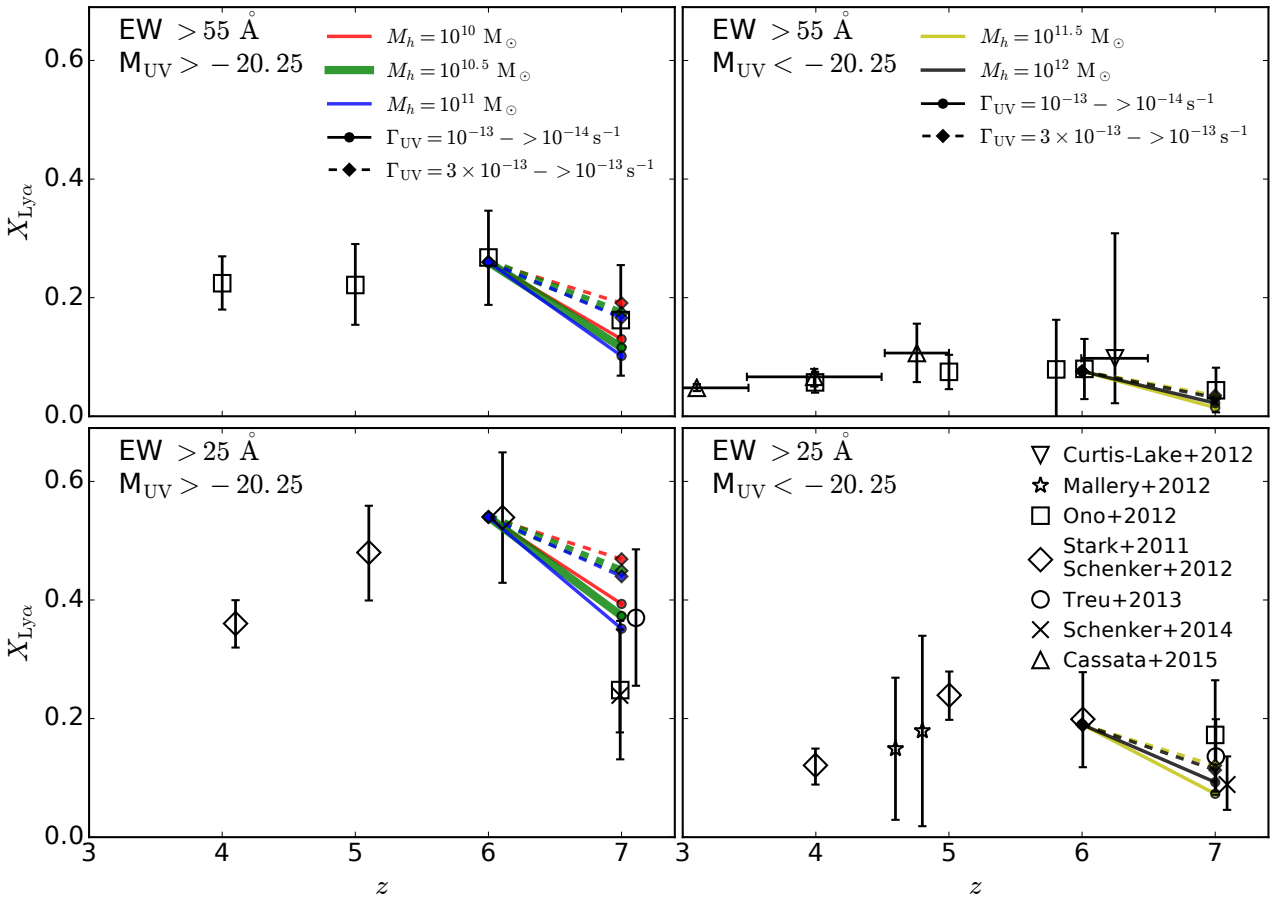

FIG. 5.— Fraction of galaxies with a Lyα equivalent width above the indicated threshold as a function of redshift. Open black symbols are the observational data points, and colored filled symbols are predictions from our LAE model. Observations are taken from Stark et al. (2011), Curtis-Lake et al. (2012), Ono et al. (2012), Mallery et al. (2012), Schenker et al. (2012), Treu et al. (2013), Schenker et al. (2014), and Cassata et al. (2015). Our model is calibrated to fit the data at $z = 6$ with the chosen value of the photoionization rate $\Gamma_{\rm UV}$ (so the agreement with data at this redshift is by construction). We show the prediction of our model for two different redshift evolution of $\Gamma_{\rm UV}$ between $z = 6$ and $z = 7$: from $10^{-13}\,{\rm s}^{-1}$ to $10^{-14}\,{\rm s}^{-1}$ (solid lines) and from $3\times10^{-13}\,{\rm s}^{-1}$ to $10^{-13}\,{\rm s}^{-1}$ (dashed lines). The decline in the Lyα fraction becomes faster as $\Gamma_{\rm UV}$ is made to also decline faster with redshift. Results are shown for low (bottom) and high (top) Lyα equivalent width thresholds and for UV-faint (left) and UV-bright (right) samples.

where the SFR is related to halo mass M_h using equation (8). We find that LAEs in halos of mass $M_h \leq 10^{11}\,M_\odot$ and $M_h > 10^{11}\,M_\odot$ correspond respectively to the UV-faint and UV-bright sample. It is worth mentioning that the $L_{\rm UV}$-M_h relation we adopt here is only used to give us a rough idea on how to separate our LAE models into UV-faint and UV-bright samples in order to compare with observations and, for this purpose, is consistent with the relation inferred from abundance matching at $z \sim 6-7$ (Trac et al. 2015).

With the assumed factor of 10 drop in $\Gamma_{\rm UV}$, we find that our model predicts a decline of a factor of 2 or less in $X_{\rm Ly\alpha}$ from $z = 6$ to $z = 7$, in good agreement with observations for both UV-faint and UV-brigth galaxies. Given that the redshift evolution of $\Gamma_{\rm UV}$ is still poorly constrained at $z \gtrsim 6$, we also show in Figure 5 the prediction of our model using a more moderate decline in $\Gamma_{\rm UV}$ from $3\times10^{-13}\,{\rm s}^{-1}$ at $z = 6$ to $10^{-13}\,{\rm s}^{-1}$ at $z = 7$ (dashed color lines). In this case, the drop in $X_{\rm Ly\alpha}$ is reduced but is still consistent with the observed evolution, especially for halos with $M_h < 10^{11}\,M_\odot$ (UV-faint LAEs) which, as we mentioned before, are the ones most affected by a change in $\Gamma_{\rm UV}$. By varying the rate of change of $\Gamma_{\rm UV}$ with redshift, we can adjust our model prediction to the observed evolution of $X_{\rm Ly\alpha}$.

We note that although $\Gamma_{\rm UV}$ can continue to increase with decreasing redshift at $z < 6$, the Lyα emission equivalent widths may no longer increase with $\Gamma_{\rm UV}$ once the infall region has been mostly ionized, if the remaining self-shielded gas is already located at a radius comparable to the aperture for the observed spectrum. Furthermore, the gas closer to the center may be ionized by the central source or by shock heating in the halo, rather than from the external ionizing background, particularly in massive halos, making the measured intensity of the Lyα emission line insensitive to the value of $\Gamma_{\rm UV}$ above a value $\sim 10^{-13}\,{\rm s}^{-1}$, which is required to ionize the infall region.

4. SUMMARY AND CONCLUSION

We construct a simple analytical model to describe the density and velocity distribution of the gas around high-redshift LAEs as a function of their host halo mass and redshift. The gas distribution is represented by a spherically symmetric cloud, consisting of the NFW profile with a core region, surrounded by an infall region and the IGM in Hubble expansion farther away from the LAE. Self-shielding on the gas distribution is computed for two values of the external ionizing background inten-

sity, which can increase rapidly as reionization proceeds. Based on detailed Lyα radiative transfer calculations, we find that this model is able to account for the observed decrease in the fraction of Lyα emitting galaxies in the interval from $z = 6$ to $z = 7$ for both UV-bright and UV-faint galaxies, if the background intensity drops moderately (by a factor $\sim 3 - 10$) over this redshift interval.

The mechanism of this model is that the rapidly growing ionizing background intensity toward $z \sim 6$ leads to a rapid ionization of the infall region surrounding LAE host halos, which greatly reduces the scattering of Lyα photons in this region. As a result, compared to the $z \sim 6$ LAEs, the Lyα photons in the red peak that are able to escape and can produce the observed Lyα emission line are much more spatially extended for $z \sim 7$ LAEs, and the detectable Lyα flux within the small central region corresponding to the commonly used observing apertures drops by a factor of a few. This provides a natural explanation for the drop in the fraction of galaxies with strong Lyα emission.

In this model, a uniform external ionizing background is adopted. During reionization, however, the UV background is expected to be highly inhomogeneous owing to the complex topology of the reionization process and the discreteness of ionizing sources (Miralda-Escudé et al. 2000; Davies & Furlanetto 2015). Inside the regions of the IGM that are highly ionized (i.e., H II regions), the local UV background can reach higher intensities than that in the neutral IGM far away from ionizing sources. This mainly happens at the early stages of reionization, before H II regions have overlapped. In the post-overlap phase of reionization, when all the low-density IGM is ionized, the spatial fluctuations in the UV background intensity are reduced, as the mean free path of ionizing photons increases rapidly (Gnedin 2000). In our model, we set the IGM environment close to LAEs as a neutral self-shielded gas, whose spatial extent is determined by the intensity of the local UV background, embedded in a large-scale ionized region. This corresponds to the late stage of reionization, which proceeds *outside-in* after the overlap of H II regions. Therefore, we believe that our adoption of a uniform background is a reasonable approximation around LAEs at $z \sim 6 - 7$, but of course improved predictions can be achieved with fully three-dimensional radiative transfer cosmological simulations.

We have not attempted to model the gas distribution inside the halo virial radius. We have simply introduced a core radius in the neutral gas distribution, ignoring the effects of complex physical processes of shock heating or internal ionization and winds, arguing that the radiative transfer process that matters for the observable Lyα emission line at the redshifts of interest occurs in the infall region and not within the virialized halo. We have also assumed a turbulent dispersion and a smooth gas distribution, and have not modeled the effects of gas inflow and outflow, a possible multiphase distribution including clumps (e.g., Dijkstra & Kramer 2012; Duval et al. 2014), and an anisotropic gas distribution (e.g., Zheng & Wallace 2014). All these factors can affect the Lyα radiative transfer and can produce anisotropic Lyα emission, which may modify the Lyα EW distribution. Our model focusing on the infall and IGM regions can be regarded as describing an average effect on the transfer of photons escaping the host halo. For future work, a detailed investigation with a more realistic gas distribution can come from modeling LAEs in high-resolution hydrodynamic galaxy formation simulations.

As a test for the uncertainty associated with the gas distribution inside halos, we have performed additional test runs by varying the key physical parameters that affect the neutral gas distribution within $r < r_h$, namely the size of the constant density core and the escape fraction of ionizing photons emitted by the LAE (see Appendix). These tests have shown that even when the neutral gas content inside the halo is much lower than in the fiducial case, our model still predicts a Lyα flux decrement from $z \sim 6$ to 7 at a level similar to that in the fiducial model. This suggests that our main results on the reduced visibility of LAEs towards $z \sim 7$ are robust even if there are uncertainties in our modeling of the neutral gas distribution within the halo, as long as a variations in the UV background intensity are able to affect the ionization state of the gas in the infall region due to self-shielding effects.

Dijkstra et al. (2007) also use the infall model of Barkana (2004) to study the IGM transmission to Lyα emission at $z \gtrsim 6$ by modifying a starting Lyα line profile based on the Lyα scattering optical depth at each frequency (i.e., the $e^{-\tau}$ model). In our work, after a self-consistent self-shielding correction, we track the scatterings of Lyα photons not only inside the halos but also in the infall regions and the IGM. The radiative transfer in the infall and IGM regions leads to additional frequency and spatial diffusion of Lyα photons that the $e^{-\tau}$ model cannot capture (e.g., Zheng et al. 2010). While the results may be qualitatively similar, our model treats in greater detail the self-shielding and radiative transfer effects.

In our model, the apparent Lyα fraction evolution is caused by the changes in neutral gas environment around LAEs induced by the rapid evolution in the UV background intensity. This rapid evolution of the UV background is expected as the mean free path of ionizing photons is quickly rising as a consequence of the reduced number density of optically thick systems towards the end of reionization (Miralda-Escudé et al. 2000). Bolton & Haehnelt (2013) also propose that the Lyα fraction evolution can be explained by the rapid change in the UV background level. Their model differs from ours in that they attribute the reduction of the LAE visibility to the generally increased number density of self-shielded regions from $z \sim 6$ to 7, whereas we propose that the main effect is due to the change in self-shielding of the infall regions around the host halos of the LAEs themselves. The models may be to some extent complementary and a combination of both reasons may provide a more complete picture on the Lyα fraction evolution at $z \gtrsim 6$ (e.g., Dijkstra 2014).

We thank Masami Ouchi and Mark Dijkstra for useful discussions. This work was supported by NSF grant AST-1208891 and NASA grant NNX14AC89G for RS and ZZ, and by Spanish grant AYA2012-33938 for JM. The support and resources from the Center for High Performance Computing at the University of Utah are gratefully acknowledged.

REFERENCES

Barkana, R. 2004, MNRAS, 347, 59
Barkana, R., & Loeb, A. 2007, Reports on Progress in Physics, 70, 627
Becker, G. D., & Bolton, J. S. 2013, MNRAS, 436, 1023
Becker, G. D., Bolton, J. S., Madau, P., et al. 2015, MNRAS, 447, 3402
Becker, G. D., Rauch, M., & Sargent, W. L. W. 2007, ApJ, 662, 72
Bolton, J. S., & Haehnelt, M. G. 2013, MNRAS, 429, 1695
Bond, J. R., Cole, S., Efstathiou, G., & Kaiser, N. 1991, ApJ, 379, 440
Bryan, G. L., & Norman, M. L. 1998, ApJ, 495, 80
Caruana, J., Bunker, A. J., Wilkins, S. M., et al. 2014, MNRAS, 443, 2831
Cassata, P., Tasca, L. A. M., Le Fèvre, O., et al. 2015, A&A, 573, A24
Calverley, A. P., Becker, G. D., Haehnelt, M. G., & Bolton, J. S. 2011, MNRAS, 412, 2543
Curtis-Lake, E., McLure, R. J., Pearce, H. J., et al. 2012, MNRAS, 422, 1425
Davies, F. B., & Furlanetto, S. R. 2015, MNRAS, 460, 1328
Dayal, P., & Ferrara, A. 2012, MNRAS, 421, 2568
Dijkstra, M., Haiman, Z., & Spaans, M. 2006, ApJ, 649, 14
Dijkstra, M. 2014, PASA, 31, e040
Dijkstra, M., & Kramer, R. 2012, MNRAS, 424, 1672
Dijkstra, M., Lidz, A., & Wyithe, J. S. B. 2007, MNRAS, 377, 1175
Duval, F., Schaerer, D., Östlin, G., & Laursen, P. 2014, A&A, 562, A52
Fan, X., Narayanan, V. K., Strauss, M. A., et al. 2002, AJ, 123, 1247
Fan, X., Strauss, M. A., Becker, R. H., et al. 2006, AJ, 132, 117
Ferrara, A., & Pandolfi, S. 2014, ArXiv e-prints, arXiv:1409.4946
Fontana, A., Vanzella, E., Pentericci, L., et al. 2010, ApJ, 725, L205
Giallongo, E., Grazian, A., Fiore, F., et al. 2015, A&A, 578, A83
Gnedin, N. Y. 2000, ApJ, 535, 530
Gunn, J. E., & Peterson, B. A. 1965, ApJ, 142, 1633
Hinshaw, G., Larson, D., Komatsu, E., et al. 2013, ApJS, 208, 19
Konno, A., Ouchi, M., Ono, Y., et al. 2014, ApJ, 797, 16
Madau, P., & Haardt, F. 2015, ApJ, 813, L8
Mallery, R. P., Mobasher, B., Capak, P., et al. 2012, ApJ, 760, 128
Meiksin, A., Bolton, J. S., & Tittley, E. R. 2014, MNRAS, 445, 2462
Mesinger, A., Aykutalp, A., Vanzella, E., et al. 2015, MNRAS, 446, 566
Miralda-Escudé, J. 1998, ApJ, 501, 15
Miralda-Escudé, J. 2003, Science, 300, 1904
Miralda-Escudé, J., Haehnelt, M., & Rees, M. J. 2000, ApJ, 530, 1
Miralda-Escudé, J., & Rees, M. J. 1998, ApJ, 497, 21
Mitra, S., Choudhury, T. R., & Ferrara, A. 2016, arXiv:1606.02719
Muñoz, J. A., Oh, S. P., Davies, F. B., & Furlanetto, S. R. 2016, MNRAS, 455, 1385
Navarro, J. F., Frenk, C. S., & White, S. D. M. 1997, ApJ, 490, 493
Neufeld, D. A. 1990, ApJ, 350, 216
Ono, Y., Ouchi, M., Mobasher, B., et al. 2012, ApJ, 744, 83
Ouchi, M., Shimasaku, K., Furusawa, H., et al. 2010, ApJ, 723, 869
Partridge, R. B., & Peebles, P. J. E. 1967, ApJ, 147, 868
Pentericci, L., Fontana, A., Vanzella, E., et al. 2011, ApJ, 743, 132
Planck Collaboration, Ade, P. A. R., Aghanim, N., et al. 2015, arXiv:1502.01589
Planck Collaboration, Aghanim, N., Ashdown, M., et al. 2016a, arXiv:1605.02985
Planck Collaboration, Adam, R., Aghanim, N., et al. 2016b, arXiv:1605.03507
Press, W. H., & Schechter, P. 1974, ApJ, 187, 425
Schaerer, D. 2003, A&A, 397, 527
Schenker, M. A., Stark, D. P., Ellis, R. S., et al. 2012, ApJ, 744, 179
Schenker, M. A., Ellis, R. S., Konidaris, N. P., & Stark, D. P. 2014, ApJ, 795, 20
Schmidt, K. B., Treu, T., Bradač, M., et al. 2016, ApJ, 818, 38
Shapley, A. E., Steidel, C. C., Pettini, M., & Adelberger, K. L. 2003, ApJ, 588, 65
Shibuya, T., Ouchi, M., Nakajima, K., et al. 2014, ApJ, 788, 74
Sobacchi, E., & Mesinger, A. 2015, MNRAS, 453, 1843
Stark, D. P., Ellis, R. S., Chiu, K., Ouchi, M., & Bunker, A. 2010, MNRAS, 408, 1628
Stark, D. P., Ellis, R. S., & Ouchi, M. 2011, ApJ, 728, L2
Stark, D. P., Richard, J., Siana, B., et al. 2014, MNRAS, 445, 3200
Tajiri, Y., & Umemura, M. 1998, ApJ, 502, 59
Trac, H., Cen, R., & Mansfield, P. 2015, ApJ, 813, 54
Treu, T., Schmidt, K. B., Trenti, M., Bradley, L. D., & Stiavelli, M. 2013, ApJ, 775, L29
Willott, C. J., Carilli, C. L., Wagg, J., & Wang, R. 2015, ApJ, 807, 180
White, R. L., Becker, R. H., Fan, X., & Strauss, M. A. 2003, AJ, 126, 1
Zheng, Z., Cen, R., Trac, H., & Miralda-Escudé, J. 2010, ApJ, 716, 574
Zheng, Z., & Miralda-Escudé, J. 2002a, ApJ, 578, 33
Zheng, Z., & Miralda-Escudé, J. 2002b, ApJ, 568, L71
Zheng, Z., & Wallace, J. 2014, ApJ, 794, 116

APPENDIX

A. MODEL UNCERTAINTIES

Our description of the the neutral gas distribution around a typical LAE at $z \gtrsim 6$ (section 2) relies on simplifying assumptions and the physical parameters of our model are poorly constrained at these redshifts. Since the Lyα radiative transfer depends critically on the neutral gas distribution around the LAE, these uncertainties in our modeling can in principle affect the resulting Lyα properties we predict. We study this effect by varying the value of various physical parameters of our model in order to quantify to what extent the uncertainties affect our final conclusion on the evolution of the Lyα fraction.

We specifically investigate the dependence on the core radius $r_{\rm core}$ as well as the escape fraction $f_{\rm esc}$ of ionizing photons emitted from the LAE. Given the computational cost associated with the Lyα radiative transfer, we perform only two test runs by increasing the value of either $r_{\rm core}$ or $f_{\rm esc}$ by a factor of two with respect to their fiducial values and only consider a halo of mass $M_h = 10^{10.5}\,{\rm M}_\odot$. For the case of a different core radius, we thus adopt the new value of $r_{\rm core} = 0.5 r_h$ while we increase $f_{\rm esc}$ to 0.2 when testing the dependence on the escape fraction. In addition, we also run an additional test to examine the impact of not including self-consistently the ionizing flux from the central source in the self-shielding correction when solving the photoionization equilibrium equation ($\Gamma_{\rm LAE} = 0$ in equation 5). Instead, for this last case, we adopt a larger core radius of $r_{\rm core} = 2/3 r_h$ to approximately account for the modified neutral gas distribution inside the halo with respect to the fiducial case.

For each of these three situations, $r_{\rm core} = 0.5 r_h$, $f_{\rm esc} = 0.2$ or $\Gamma_{\rm LAE} = 0$, we calculate again the corresponding neutral gas distributions, Lyα spectra and the evolution of the Lyα fraction predicted by our model when we vary the UV background intensity from $\Gamma_{\rm UV} = 10^{-13}\,{\rm s}^{-1}$ at $z = 6$ to $\Gamma_{\rm UV} = 10^{-14}\,{\rm s}^{-1}$ at $z = 7$, and compare the results with the fiducial case.

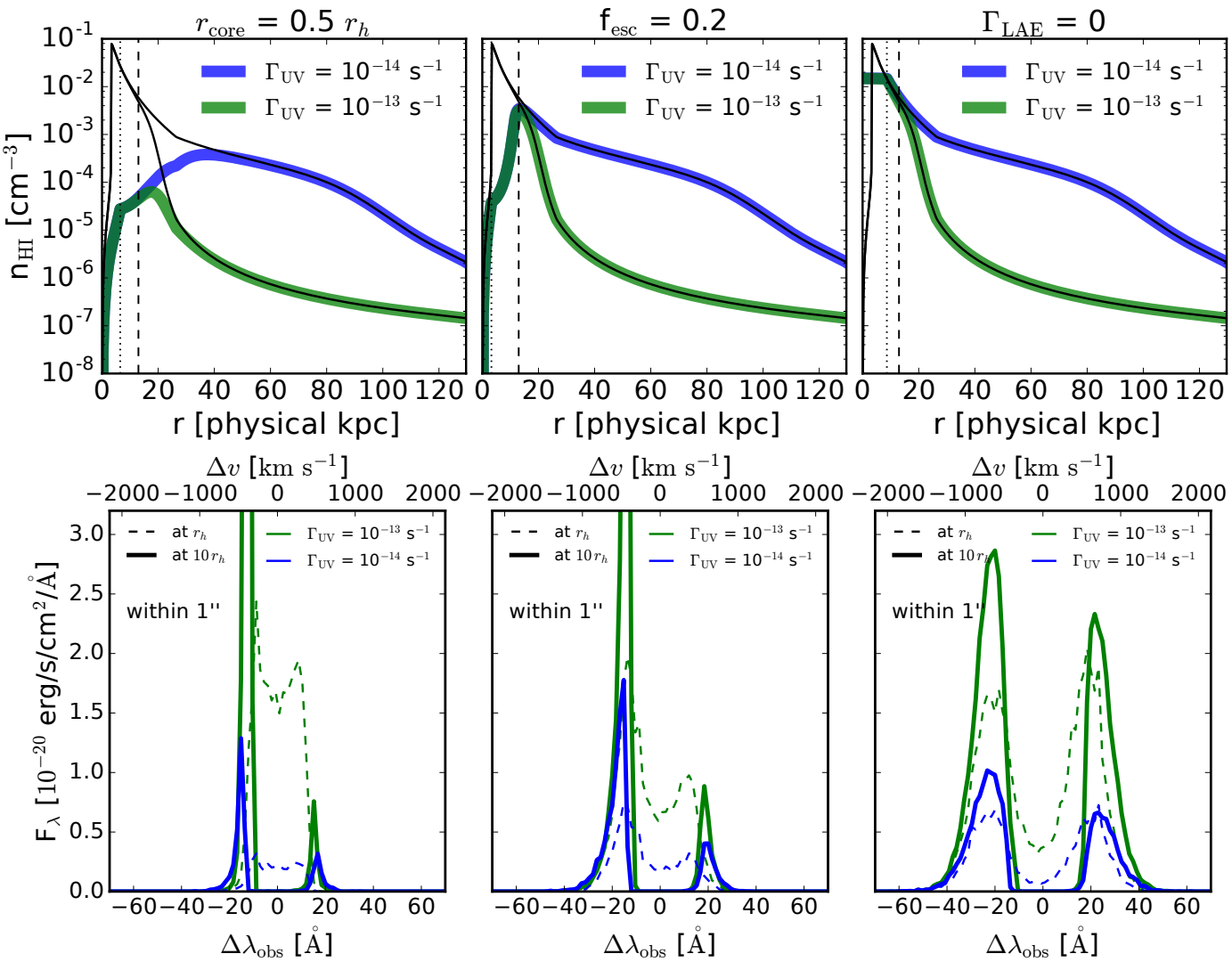

FIG. A1.— Resulting neutral gas profiles (*top*) and Lyα spectra for photons escaping within 1″ from the central source (*bottom*) after varying some physical parameters of our model for a halo of mass $M_h = 10^{10.5}\,{\rm M}_\odot$. The different lines have similar meaning as in Figures 1 and 2, except for the solid black lines in the top panels which show the neutral gas profile of our fiducial model for comparison (see Fig. 1). The first column shows the effect of adopting a larger core radius of $r_{\rm core} = 0.5r_h$ while the second column corresponds to an increase in the escape fraction of ionizing photons from $f_{\rm esc} = 0.1$ to 0.2. In the third column, we show the situation where the ionizing flux from the central source is not included in the photoionization equilibrium equation ($\Gamma_{\rm LAE} = 0$ in equation 5). Note that for this latter case, we also increase the value of the core radius (see text).

A.1. *Effects on the neutral gas distributions*

The top panels of Figure A1 show the neutral gas profiles obtained for the different test runs described above. The black solid lines are the profiles corresponding to the fiducial model presented in Figure 1 for comparison. We find that increasing either $r_{\rm core}$ or $f_{\rm esc}$ makes it easier for photons emitted from the central LAE source to affect the ionization state of the gas out to larger radii as compared to the fiducial model in which these photons are all absorbed at $r < r_{\rm core}$ to ionize the gas within the core. Instead, in the the case of a higher $f_{\rm esc}$, the central source is able to maintain most of the gas inside the halo ($r < r_h$) ionized with a peak neutral gas density ~ 30 times lower than in the fiducial case. In the case of a larger core radius, photons emitted from the LAE can reach even larger radii and ionized the gas out to $\sim 1.5r_h$ simply because the total gas density is much lower than in the fiducial model for $r < 0.5r_h$. In all the test cases however, we find that the ionization state of the infall region ($2r_h < r < 6r_h$) is largely unaffected compared to the fiducial situation and is mostly governed by the value we assume for the intensity of the external UV background.

A.2. *Effects on the Lyα spectra*

The resulting Lyα spectra corresponding to our three test runs are shown in the bottom panels of Figure A1 and the different lines have the same meaning as in Figure 2. Since the aperture commonly used for LAE detection at $z \gtrsim 6$ is $\sim 1''$ (Section 3.1), we only show the spectra for photons that escape within a projected radius of 1″ which can be directly compared to the spectra obtained for our fiducial model presented in the right panel of Figure 2 (although note the slightly smaller range of the y-axis used here). In the cases of a larger $r_{\rm core}$ or $f_{\rm esc}$, the overall main differences seen in the Lyα spectra

compared to the fiducial case are: (1) a smaller offset from the line center of the blue and red peak for both sets of spectra emerging from either r_h (dashed lines) or $10r_h$ (solid lines) and (2) an enhanced asymmetry of the blue peak with respect to the red peak in the final spectra emerging at $10r_h$. Both of these effects result from the smaller H I column density inside $r < r_h$ (top panels of Figure A1) which reduces the Lyα optical depth and thus the number of scattering experienced by Lyα photons as they diffuse out of the halo with respect to the fiducial case. This is especially visible in the case of $r_{\rm core} = 0.5r_h$ for which a large number of photons are able to escape the halo with frequencies close to the line center and the spectra emerging from r_h appear relatively flat. As a consequence of the halo being more optically thin to Lyα photons, the bulk flow of the gas in the infall region (which remains largely unaffected) imprints more effectively the typical asymmetry between the blue and the red peak as expected for a source within a collapsing gas cloud (e.g. Zheng & Miralda-Escudé 2002a).

A.3. *Effects on the Lyα fraction evolution*

We now examine the redshift evolution of the Lyα fraction predicted by our three test runs. The Lyα fraction is computed using the same method as described in Section 3.3 by assuming that the intensity of the ionizing background drops from $\Gamma_{\rm UV} = 10^{-13}\,{\rm s}^{-1}$ at $z = 6$ to $\Gamma_{\rm UV} = 10^{-14}\,{\rm s}^{-1}$ at $z = 7$. Figure A2 shows the resulting Lyα fraction evolution for the two equivalent width threshold, $W_t = 55$ Å (left) and $W_t = 25$ Å(right) for the 3 test cases (thin color lines) as well as for the fiducial model (thick black line) for comparison. Observational data points (open black symbols) are the same as in the left panels of Figure 5 for UV-faint ($\rm M_{UV} > -20.25$) galaxies which corresponds to the halo mass of $M_h = 10^{10.5}\,{\rm M}_\odot$ that we consider here. We see that increasing $r_{\rm core}$ or $f_{\rm esc}$ by a factor of 2 still results in the same decline of the Lyα fraction between $z = 6$ and $z = 7$ as in the fiducial case, which shows that the drop in Lyα flux predicted by our model is robust despite the uncertainties in modeling the neutral gas distribution within $r < r_h$.

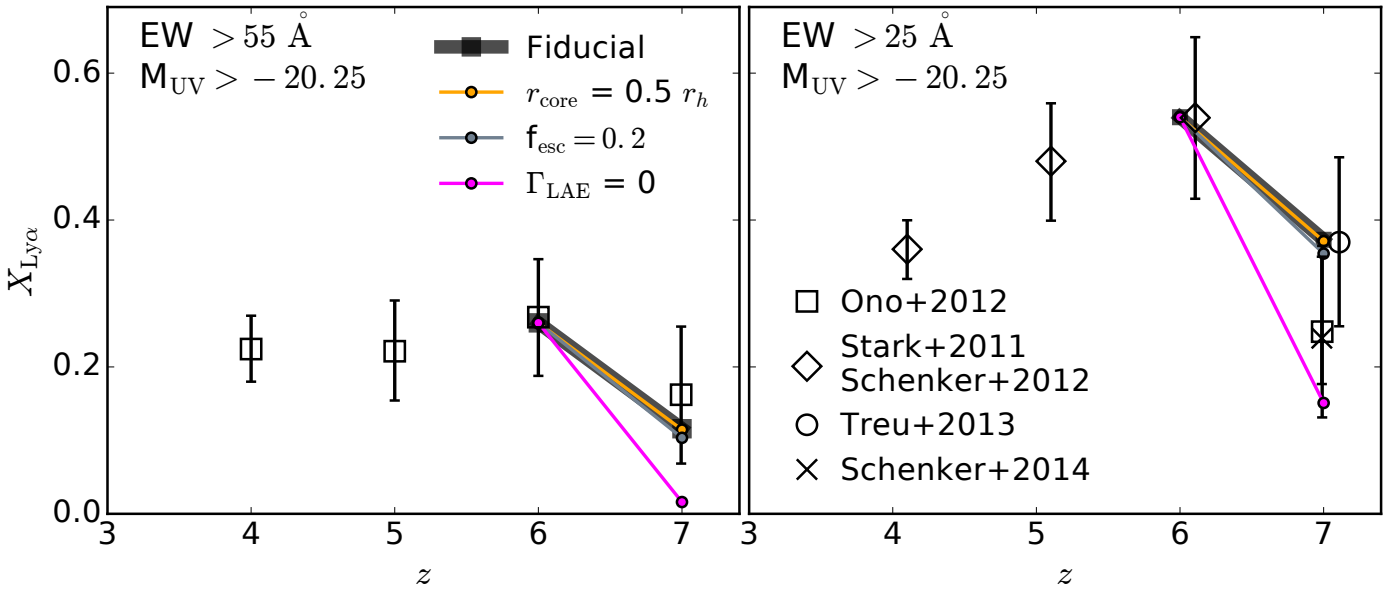

FIG. A2.— Lyα fraction evolution predicted by our model after varying the physical parameters corresponding to the different cases shown in Fig. A1 for a halo of mass $M_h = 10^{10.5}\,M_\odot$ and for the two equivalent width thresholds commonly considered in LAE surveys. Data points (open black symbols) correspond to the the observed Lyα fraction evolution for UV-faint galaxies ($M_{UV} > -20.25$, as in the left panels of Fig. 5). The evolution predicted by our fiducial model is shown as a thick black line with square symbols for comparison. Increasing the size of the core or the escape fraction by a factor of 2 has no noticeable effect on the Lyα fraction evolution indicating that our results seem robust against uncertainties in the modeling.